Construction and Building Materials 153 (2017) 55–68

Contents lists available at ScienceDirect

Construction and Building Materials

journal homepage: www.elsevier.com/locate/conbuildmat

Experimental and numerical study of effective thermal conductivity of cracked concrete

Lei Shen [a,b], Qingwen Ren [c,*], Linfei Zhang [a], Yan Han [c], Gianluca Cusatis [b]

[a] Hohai University, Hydraulic Structure, Nanjing 210098, China
[b] Northwestern University, Civil and Environmental Engineering Department, Evanston 60208, USA
[c] Hohai University, Engineering Mechanics, Nanjing 210098, China

HIGHLIGHTS

- Simulations show concrete thermal conductivity has a decrease of 20–30% during tensile and compressive failure.
- Debonding of aggregate and mortar dominants the reduction of concrete thermal conductivity.
- Experiments show a 25% decrease in thermal conductivity during compressive test.
- Wang Jiajun model is calibrated to calculate the thermal conductivity of cracked concrete.

ARTICLE INFO

Article history:
Received 8 February 2017
Received in revised form 4 June 2017
Accepted 4 July 2017
Available online 15 July 2017

Keywords:
Cracked concrete
Effective thermal conductivity
Mini-scale modeling
Finite element method
Experiment
Wang Jiajun model

ABSTRACT

The pronounced decrease of Effective Thermal Conductivity (ETC) due to the cracking behavior of concrete changes the temperature profile in concrete structures, indirectly inducing the redistribution of thermal stresses. To study this phenomenon, a mini-scale numerical method within the framework of finite element method is proposed for both tensile and compressive cracked concrete and this method is applied to obtain quantitative relationships between tensile or compressive strain and ETC. Results show that (a) for tensile dominated failure, concrete ETC decreases by 23% during the plastic stage whereas little decrease is found at complete failure; (b) for compressive dominated failure, ETC decreases by 30% during the plastic stage, and then becomes stable afterwards. In the softening stage ETC linearly decreases with the increase of compressive strain; (c) it is the interfacial thermal resistances induced by the micro-cracks between aggregates and mortar rather than the macro-cracks that play the dominant role in this phenomenon; (d) concrete ETC becomes anisotropic when cracks appear. The experiments show that compressive cracked concrete's ETC vertical to cracks dramatically decreases by 20–25% at plastic drop stage and then becomes stable at the plastic steady stage. The numerical results are used to determine the interfacial thermal resistance factor in Wang Jiajun model. The proposed formulation provides results that are in excellent agreement with experiments.

1. Introduction

It is acknowledged that cracking behavior in massive concrete structure is inescapable, especially for hydraulic engineering and nuclear reactor structures [1]. Many researchers put their efforts on the influence of cracks on the safety and water retaining performance of dams while little attention has been paid so far to the effects of cracks on temperature distribution. Thermal loads induced by hydration reaction of cement paste and cold weather as well are a common reason for cracking in hydraulic structures [2]. Hence it is of vital importance to study the cracks' influence on the thermal distribution in the massive concrete structure.

According to Fourier's Law and energy conservation law, the accuracy of numerical studies primarily relies on two input thermal parameters, i.e., thermal conductivity and specific heat capacity. However, recent experimental investigations [3–5] showed that, after the occurrence of concrete cracking, specific heat capacity was proved to remain unchanged, while the thermal conductivity decreased significantly. Therefore studying the evolution of thermal conductivity during concrete failure is the main objective of this study.

Numerical investigations in recent years have increased the understanding of this topic. Tang et al. [6] found out by using the

* Corresponding author.
E-mail address: renqw@hhu.edu.cn (Q. Ren).

http://dx.doi.org/10.1016/j.conbuildmat.2017.07.038
0950-0618/

RFPA2D program [7,8] that for uniaxial compression tests the maximum drop of effective thermal conductivity (ETC) of a concrete specimen was 24% during softening. In their finite element method (FEM) based program, the elements' thermal conductivity was set to zero when the compressive or tensile stress reached the peak value. Obviously, this assumption did not correctly reflect the thermal behavior inside cracks. Hence Shen et al. [9] proposed a mini-scale numerical method to simulate the thermal conductivity of tensile cracked concrete. In this work, the heat bridge effect, caused by the higher conductivity of aggregates, and the interfacial thermal resistance effect, induced by the rupture of aggregates and mortar were emphasized to be the main mechanism of the remarkable drop of conductivity (23%) during the plastic stage. Wu et al. [10] also found the debonding of aggregate and mortar would lead to a temperature jump across the micro-cracks at Interfacial Transition Zone (ITZ). Therefore numerical study on this topic should be carried out at mini scale in order to capture the debonding phenomenon of aggregate and mortar.

Numerical simulations, coupled with experiment, are considered to be an effective and efficient tool for successfully examining material properties. Hence experimental investigations are necessary. Vejmelkova et al.'s [4] experiment showed up to 40% decrease in thermal conductivity in cracked concrete specimens which were heated up to 600 °C to impose randomly distributed cracks. Perkowski [11] analyzed the variation of thermal conductivity due to brittle damage in concrete subjected to the ultimate compression load and observed an average of 20% decrease in thermal conductivity for high-performance concrete specimens. The aforementioned experiments have two shortcomings: one is that the thermal conductivity evolution could not be obtained, and another one is that measurements of conductivity are taken place after unloading when cracks undergo unloading and closure.

In the current study, three-dimensional simulations of heat transfer at mini scale and experiments of compressive cracked concrete ETC are carried out. Then a semi-theory model is calibrated by numerical results and compared to experimental data.

2. Numerical method and results

Concrete has a highly heterogeneous microstructure and its composite behavior is exceedingly complex. Therefore, reliable predictions of the behavior of the material based exclusively on experimental studies have become limited. For obtaining a deeper understanding, FEM-based simulations at mini scale have been employed to study the macroscopic constitutive mechanical [12] and thermal behavior of concrete [13] and their coupling mechanism [7–9].

At mini scale, concrete is considered as a three-phase composite material consisting of mortar matrix, aggregate, and ITZ. Material properties of different phases are directly assigned to the elements in order to characterize the random heterogeneity in concrete numerically. The ability of this numerical approach has been validated by good agreements between experimental data and numerical results [9,10,14,15]. One point should be highlighted that some authors use the term "meso-scale" (no ITZ) in a wider sense to include the "mini-scale" [16–19] (see Fig. 1).

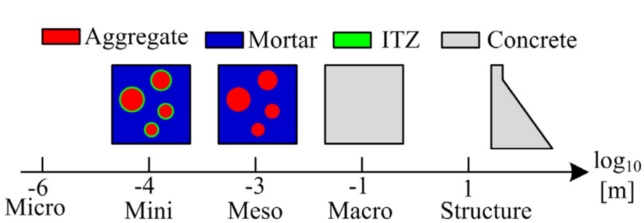

Fig. 1. Illustration of concrete material at multi scale.

2.1. Mini-scale numerical method

The first step is to obtain the crack information of concrete during low friction uniaxial tension and compression tests. The three phases, namely mortar, aggregate and ITZ, are simulated by concrete damage plastic (CDP) model with different parameters given in Section 2.2. The constitutive is basically introduced in Section 2.1.1 which is provided by commercial finite element software ABAQUS [20].

Secondly, thermal conductivity of each element is modified with respect to its cracking opening which is obtained from the first step. The details of thermal behavior in crack are discussed and the modifier formulas for three cracked phases are assumed in Section 2.1.2.

The last step is to calculate the macroscopic ETC of concrete specimen with modified thermal conductivity distribution. The homogenization method is proposed in Section 2.1.3. By repeating these three steps above, one can obtain the evolution of ETC during tensile and compressive failure.

2.1.1. Concrete damage plastic model

Mechanical behavior of concrete-like material, e.g., cracking in tension and crushing in compression, can be well simulated by using CDP model [14,21,22]. The CDP model was first proposed by Lubliner et al. [23] for monotonic loading, and was further developed by Lee and Fenves [24] to consider the dynamic and cyclic loadings. The basic framework of the CDP model is illustrated as follows.

The uniaxial stress-strain curves can be converted into stress versus plastic strain curves. Tensile damage factor d_t and compressive damage factor d_c are assumed as increasing functions of the equivalent plastic strain ($\tilde{\varepsilon}^{pl}$), $\tilde{\varepsilon}_t^{pl}$ and $\tilde{\varepsilon}_c^{pl}$ (subscripts, 't' and 'c' stand for tension and compression, respectively). Herein, the degradation of the elastic stiffness is characterized by damage variables, d_t and d_c, and the stress-strain relationships (shown in Fig. 2) under tension and compression are:

$$\begin{aligned} \sigma_t &= (1 - d_t)E_0(\varepsilon - \tilde{\varepsilon}_t^{pl}) \\ \sigma_c &= (1 - d_c)E_0(\varepsilon - \tilde{\varepsilon}_c^{pl}) \end{aligned} \tag{1}$$

respectively, in which E_0 is the initial (undamaged) elastic modulus, σ is stress and ε is strain. The evolution equation of the hardening parameters subjected to multi-axial loading are developed from

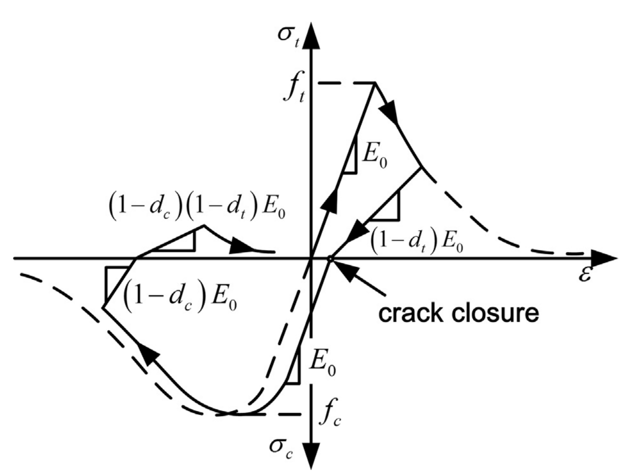

Fig. 2. Unaxial loading path of CDP model. f_c is usually 10 times of f_t.

uniaxial loading conditions. For more detail about the constitutive model, please refers to Lubiner et al. [23] and Lee and Fenves [24].

2.1.2. Thermal behavior in cracks

Heat exchange in cracks is very complex and includes not only heat conduction, but also convection and radiation as discussed below.

For a cube specimen with 2 W/(K·m)$^{-1}$ thermal conductivity, 100 mm side length and 20 °C temperature difference along the sides, the conductive heat flux ϕ_{con} equals to 4 W.

To calculate the flux caused by convection and radiation, crack surfaces are assumed as a pair of parallel surfaces (see in Fig. 3) and crack opening, δ, is set as 1000 μm (1% of 100 mm) which is very huge for massive concrete structures. Hence when heat flux becomes steady, the linear temperature difference, ΔT, between crack surfaces will be 0.2 K (1% of 20 K). Then the Grashof number (Gr), a dimensionless number in fluid dynamics and heat transfer, is introduced to approximate the ratio of the buoyancy to viscous force acting on a fluid. For air in crack, the finite space Gr empirical formula is [25]:

$$Gr = \frac{g\alpha\Delta T\delta^3}{\mu^2} = 1.88 \tag{2}$$

where $g = 10\ \mathrm{m/s^2}$ is gravitational acceleration; $\alpha = 2.41 \times 10^{-3}\ \mathrm{K^{-1}}$ is air volume expansion coefficient; $\mu = 16 \times 10^{-6}\ \mathrm{m^2/s}$ is air Kinematic viscosity. If Gr is larger than 2860 (for vertical crack) or 2430 (for horizontal crack), the free-convection behavior of air should be considered [25]. Obviously, the Gr in cracks is much less than these thresholds which means that the space inside crack is too narrow for air to convect. In addition, no forced convection is considered in this study. Therefore the convection can be neglected.

Another heat exchange mechanism is radiation. In engineering calculation, concrete can be regarded as a gray body when its temperature is under 2000 K [25]. Hence, the radiant heat flux, ϕ_{rad}, between the two crack surfaces can be expressed as:

$$\phi_{rad} = \frac{C_0\left[\left(\frac{T_1}{100}\right)^4 - \left(\frac{T_2}{100}\right)^4\right] \times S}{\frac{1}{\varepsilon_{rad}} + \frac{1}{\varepsilon_{rad}} - 1} \tag{3}$$

where $\varepsilon_{rad} = 0.8$ is concrete's radiant emittance at 20 °C; $C_0 = 5.67\mathrm{W/(m^2 \cdot K^4)}$ is black body radiation coefficient; $S = 10^{-2}\ \mathrm{m^2}$ is specimen's section area. When the ambient temperature is 20 °C, $T_1 = 293.2\ \mathrm{K}$ and $T_2 = 293\ \mathrm{K}$. And then the ϕ_{rad} equals to 0.0076 W, which is 0.2% of ϕ_{con}. Therefore, the neglecting of radiant heat exchange is reasonable in this investigation.

In summary, the conduction dominates the heat transfer in concrete cracks at ambient temperature. So the relationships between cracking extent and thermal conductivity in phases' finite elements are given in this Section, since pertinent experimental data is not available so far. The tensile equivalent plastic strain ($\tilde{\varepsilon}_t^{ck}$) is employed to depict cracking degree of elements, and the thermal conductivity is considered as an $\tilde{\varepsilon}_t^{ck}$ -dependent isotropy parameter.

Since the ITZ is thin (50 μm) enough to be regard as an interface, the ITZ elements' conductivity λ_{ITZ}^{ck} turns to that of the air λ_{air} when air flow into the gaps between aggregate and mortar matrix. During the failure process, when cracks propagate into mortar matrix and aggregates, the defects are assumed to be smeared in elements and the values of thermal conductivity satisfy the series model.

$$\begin{aligned} &\lambda_{ITZ}^{ck} = \lambda_{air} \\ &\frac{1+\tilde{\varepsilon}_t^{ck}}{\lambda_{cem}^{ck}} = \frac{1}{\lambda_{cem}} + \frac{\tilde{\varepsilon}_t^{ck}}{\lambda_{air}} \\ &\frac{1+\tilde{\varepsilon}_t^{ck}}{\lambda_{agg}^{ck}} = \frac{1}{\lambda_{agg}} + \frac{\tilde{\varepsilon}_t^{ck}}{\lambda_{air}} \end{aligned} \tag{4}$$

where the subscripts 'ITZ', 'agg', 'cem' and 'air' mean ITZ, aggregate, cement and air, respectively and the superscript 'ck' represents cracked; the tensile equivalent plastic strain in CDP model, which has similar conception with the inelastic strain in discrete model [18] and fracture model [8], is defined as (Fig. 4) [20]:

$$\tilde{\varepsilon}_t^{ck} = \tilde{\varepsilon}_t - \frac{\sigma_t}{E_0} \tag{5}$$

2.1.3. ETC calculation strategy

Computational homogenization is a multi-scale approach where the macro-scale material response is obtained from an Representative Volume Element (RVE). A sample from the heterogeneous material qualifies as an RVE when it is small enough compared to the macrostructural dimensions, yet it contains sufficient statistical information about the microstructure so as to accurately represent the response that the heterogeneous material exhibits at the macro-scale [9,12,13]. Hence the side length of concrete RVE is usually at least 100 mm [26]. In computational thermal homogenization, an effective thermal conductivity matrix $\boldsymbol{\lambda}$ is introduced to map the volume average of temperature gradient $\langle\nabla\mathbf{T}\rangle$ to the volume average of thermal flux $\langle\mathbf{Q}\rangle$:

$$\langle\mathbf{Q}\rangle = -\boldsymbol{\lambda}\langle\nabla\mathbf{T}\rangle \tag{6}$$

where the volume average of a quantity $\langle\cdot\rangle$ is defined as:

$$\langle\cdot\rangle = \frac{1}{|\Omega|}\int_\Omega \cdot\, \mathrm{d}\Omega \tag{7}$$

with Ω is the RVE volume.

For the heterogeneous material with isotropic ETC λ_{iso}, the Eq. (6) can be written as:

$$\langle\mathbf{Q}\rangle = -\begin{bmatrix} \lambda_{iso} & & \\ & \lambda_{iso} & \\ & & \lambda_{iso} \end{bmatrix}\langle\nabla\mathbf{T}\rangle \tag{8}$$

and in 3-D problem, the λ_{iso} becomes:

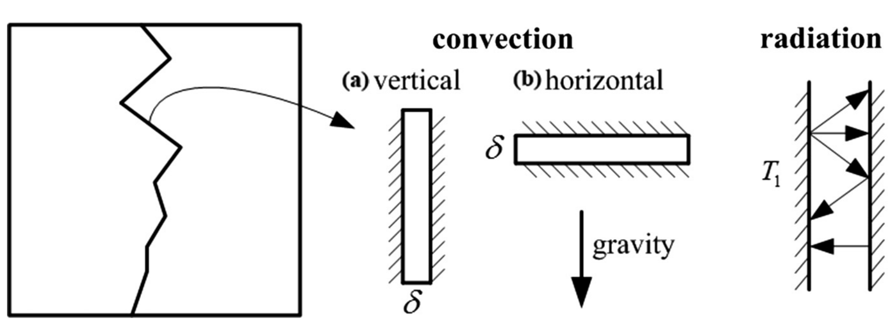

Fig. 3. Illustration for heat exchange in crack.

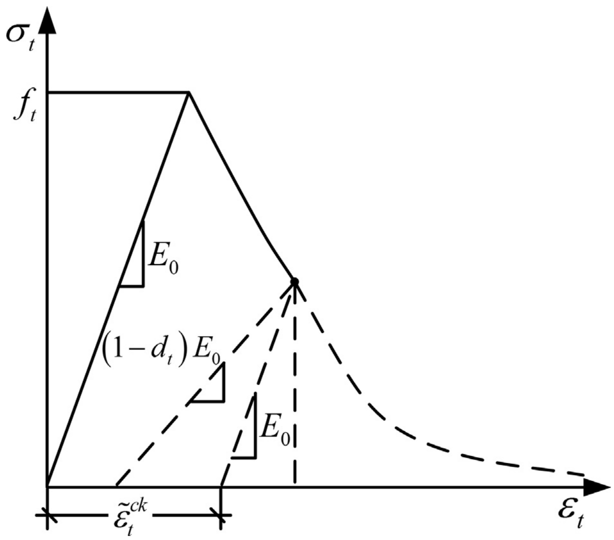

Fig. 4. Tensile equivalent plastic strain in CDP model.

$$\lambda_{iso} = -\frac{\langle \mathbf{Q} \rangle_1 \langle \nabla \mathbf{T} \rangle_1 + \langle \mathbf{Q} \rangle_2 \langle \nabla \mathbf{T} \rangle_2 + \langle \mathbf{Q} \rangle_3 \langle \nabla \mathbf{T} \rangle_3}{\langle \nabla \mathbf{T} \rangle_1^2 + \langle \nabla \mathbf{T} \rangle_2^2 + \langle \nabla \mathbf{T} \rangle_3^2} \tag{9}$$

In this study, to satisfy the Hill criterion, a linear temperature boundary condition with a constant prescribed temperature gradient $\nabla \mathbf{T}_1$ is addressed in direction 1, so that $\langle \nabla \mathbf{T} \rangle_1 = \nabla \mathbf{T}_1$ and $\langle \nabla \mathbf{Q} \rangle_1 = \nabla \mathbf{Q}_1$ can be proved. Above all the ETC in 1-D can be simplified as follows (see Fig. 5):

$$\lambda_1 = -\frac{\langle \mathbf{Q} \rangle_1}{\langle \nabla \mathbf{T} \rangle_1} = -\frac{\mathbf{Q}_1}{\nabla \mathbf{T}_1} \tag{10}$$

2.2. Specimens and parameters

The take-and-place method [12] which follows Fuller Curve (the shape factor is 0.5) is used to randomly place sphere aggregates (diameter ranges from 30 mm to 10 mm) into the 100 mm side length cube specimen. Fig. 6 shows the 40% aggregate volume fraction (AVF) specimen composed of mortar (blue phase), aggregate (red phases) and ITZ (green phases). No defect is set for triggering cracks localization.

For the three-dimensional simulations, two bottlenecks need to be broken through. One is the method used to mesh the ITZ mesh which will be discussed in Section 2.3, and the another one is the definition of the ITZ mechanical properties because these properties still cannot be measured directly.

Xiao et al. [27] reported that on the basis of nanoindentation tests, the thickness of ITZ is in the range 40–65 μm and the average indentation modulus of ITZ is 70–90% of that of mortar matrix. Hence in this numerical study, a reduction factor of ITZ mechanical properties is assumed to be 0.8 (listed in Table 1) compared to those of mortar. To alleviate mesh sensitive results, the post-failure tensile behavior is defined by using the fracture energy cracking criterion that employs a stress-displacement curve, rather than a stress-strain curve, to depict tensile behavior after cracking. The ultimate displacement of ITZ is given to obtain proper fracture energy, ranging from 49.6 to 62 N/m (in Section 2.4.1), in macro stress strain response [28]. In addition, a residual strength (0.2 MPa) is suggested for ITZ to avoid convergence problem caused by the distortion of cracked ITZ element during failure.

For each AVF (30%, 35% and 40%), the tensile and compressive tests of two specimens with different aggregates distribution are modeled in X and Y directions (Cartesian coordinates in Fig. 6). The averages value of tests in different directions are used in plots.

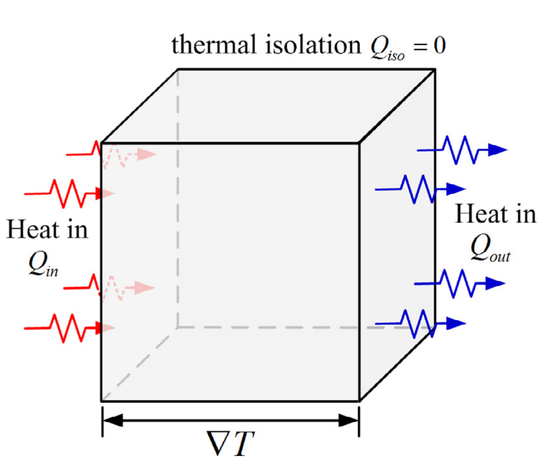

Fig. 5. Illustration of the principle of the ETC computation.

2.3. Aggregate-expansion method

The ITZ meshing method in three-dimensional remains a challenging issue since ITZ is only 40–65 μm thick [27], which is rather small compared to the general dimensions of coarse aggregates (at least 5 mm in diameter) in typical concrete laboratory specimens. The correct ITZ thickness is of vital importance to correctly simulate the mechanical and thermal behavior of concrete; however the thinner the ITZ elements are, the higher the computational demands is.

In the previous mini-scale analysis, the ITZ structure was represented by either zero-thickness interface elements [10] or brick elements larger than actual ITZ size (background method) [15] about 500–1000 μm in thickness. Both methods resulted in big discrepancies in the dimensions of ITZ between the models and the real structures, necessarily inducing a low accuracy in the simulations.

Accordingly, Li et al. [29,30] proposed “Aggregate-Expansion Method” (AEM) in which the ITZ structure is represented with 50 μm thickness wedge elements in an acceptable number. AEM can generate the thin-layer elements between aggregate and mortar meshes. A brief overview of the procedure is as follows:

(1) Generate a grid model without ITZ elements (see in Fig. 7a): mesh a aggregates and mortar with tetrahedron elements.
(2) Select “Old ITZ Nodes”: select the nodes at the interface between mortar (blue) and aggregate *i* (red), named “Old ITZ Nodes”.
(3) For aggregate *i*, select the mortar elements which contains “Old ITZ Nodes”.
(4) Generate “New ITZ Nodes”: for aggregate *i*, extend the Old ITZ Nodes by 50 μm outward the aggregate surface in the radial direction, named “New ITZ Nodes”.
(5) Generate the new mortar elements: update the mortar elements by replacing “Old ITZ Nodes” with paired “New ITZ Nodes”.
(6) Obtain the ITZ elements: organize the Old ITZ Nodes (shared by aggregate and ITZ elements) and New ITZ Nodes (shared by mortar and ITZ elements) into wedge ITZ elements (green, see in Fig. 7b).

One need to be pointed out that to ensure the quality of ITZ elements the aspect ratio of wedge elements is recommended as 1:40, which is limited to be no less than 1:50 in ABAQUS [20,31]. Hence

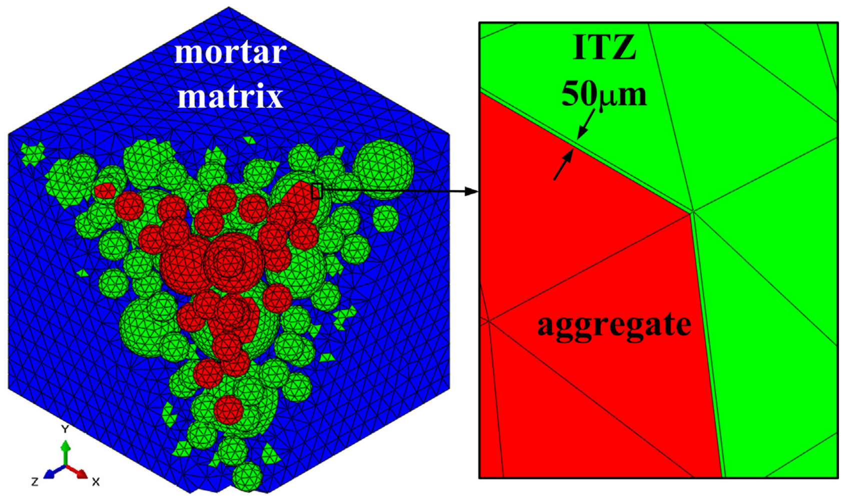

Fig. 6. 40% AVF mini-scale concrete specimen.

Table 1
Parameters in simulation.

Material	Aggregate	Mortar matrix	ITZ	Air	Reference
Elastic models E / (GPa)	50	20	16		[2,14]
Poisson's ratio	0.16	0.22	0.2		
Tensile strength f_t/(MPa)	15	3	2.4		
Compressive strength f_c/(MPa)	200	40	32		
Ultimate displacement w_c/(μm)	50	40	20		
Thermal conductivity λ/(W/(m·K))	5	2	2	0.026	[2,6,25]

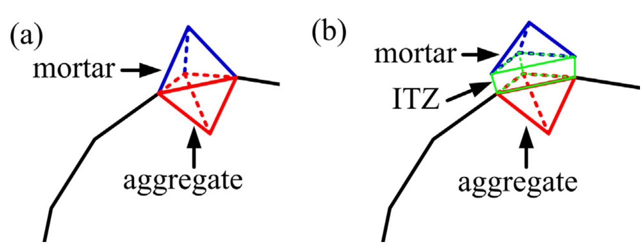

Fig. 7. Aggregate-expansion method: (a) Before meshing and (b) After meshing.

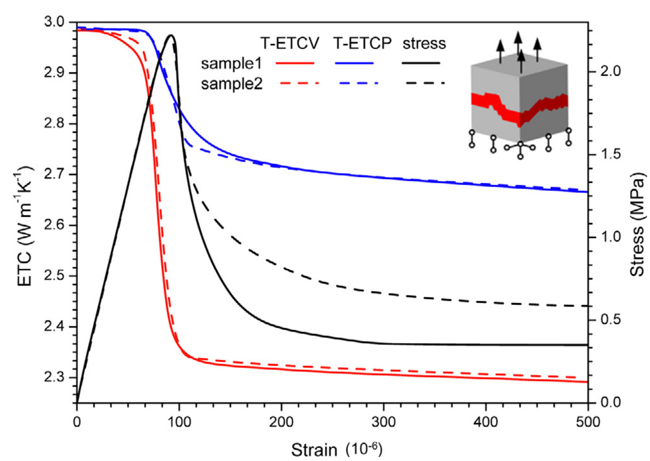

Fig. 8. Relationship between tensile strain and ETC.

the number of elements for the specimen in Fig. 6 is about 300 thousands.

2.4. Numerical results

2.4.1. Tension

Fig. 8 shows the numerical complete tensile stress-strain curves (black) and the relationships between tensile strain and tensile cracked concrete ETC vertical to cracks (T-ETCV in red) or tensile cracked concrete ETC parallel to cracks (T-ETCP in blue) respectively. At the tension stiffening stage (0–80 μ-strain), the stress linearly increases with strain. Before the peak, plastic strain can be observed in the range 80–100 μ-strain and micro-cracks initiate at ITZ (Fig. 9b). With the accumulation and propagation of micro-cracks, the specimen reaches its peak stress at 2.24 MPa and at this point the displacement distribution becomes discontinuous (Fig. 10b). Then in the softening phase, the tensile stress decreases rapidly with the growth of a macro-crack. At 500 μ-strain, the specimen reaches its tensile residual stress and ultimately fractures into two halves (Fig. 10c). Overall, this specimen shows strong brittleness in tension.

According to the tensile failure process, the evolutions of T-ETCV and T-ETCP, can be divided into 3 stages with respect to tensile strain. In the elastic stage, ETC has a little change. In the plastic stage (80–100 μ-strain) both the ETCV (23%) and ETCP (10%) have a significant reduction, while at the softening stage a very slight linear decrease appears.

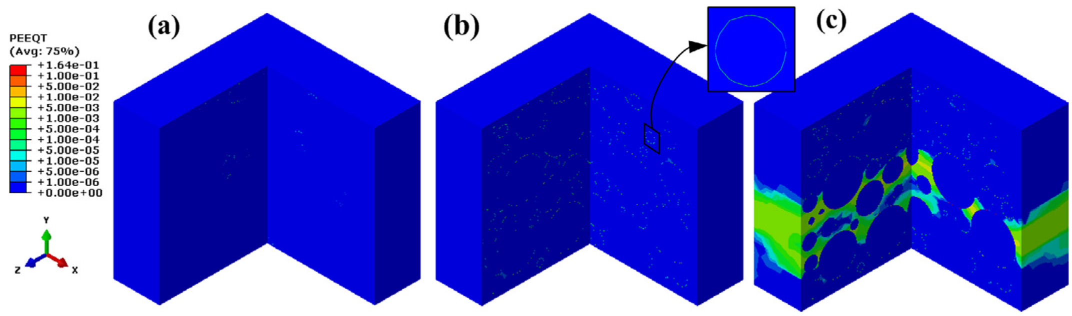

Fig. 9. PEEQT($\tilde{\varepsilon}_t^{ck}$ in ABAQUS) distribution during the tensile test: (a) 76 μ-strain, (b) 100 μ-strain and (c) 500 μ-strain.

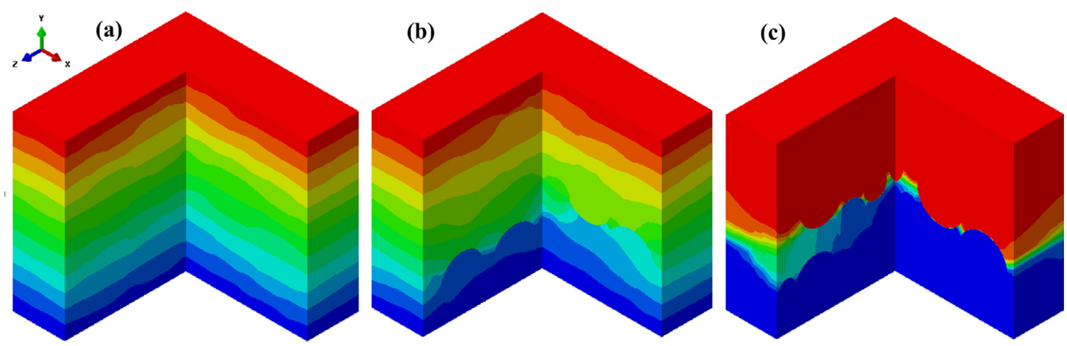

Fig. 10. Y-displacement distribution during tensile test: (a) 76 μ-strain, (b) 100 μ-strain and (c) 500 μ-strain.

The variation of thermal conductivity is highly consistent with the failure process. The initiation, accumulation, propagation and coalescence of cracks directly reduce the local thermal conductivity inside the specimen. In Fig. 11a, one can see that the ITZ first cracked at the two opposite ends of aggregates in the Y (loading) direction where the thermal conductivity of cracked ITZ elements becomes that of air (blue). Then as the load increases, cracks propagate along the surface of aggregates (Fig. 11b). In the softening stage, the thermal conductivity of most ITZ elements decreased to that of air around the macro-crack (Fig. 11c). Ultimately, when the tensile strain reaches 500 μ-strain, the conductivity of cracked mortar elements decreases to various degrees with the crack opening at the location of the macro-crack.

Fig. 12 illustrates the thermal conductivity distribution of the tensioned 500 μ-strain specimen. In this figure, the thermal conductivity of elastic aggregates elements (gray), uncracked mortar (red) and ITZ elements (red) remains unchanged, the conductivity of cracked ITZ elements (blue) turns into that of air and at the zone of macro-crack the conductivity of cracked mortar elements decreases to various degrees with the crack opening.

Since the thermal conductivity of aggregates is usually 2.5 times of that of mortar, heat prefers to flow in and out of the aggregates while passing the specimen. Thus in Fig. 13a, heat shortcuts provided by aggregates can be easily observed which in this study is called "heat bridge effect" (red lines). When mortar and aggregates start to debond, the heat will be prevented by air the in cracked ITZ (Fig. 13b). This phenomenon significantly weakens the "heat bridge effect", leading to a remarkable drop of conductivity in the plastic stage. Herein this is called "interfacial thermal resistance (ITR)" effect.

In Figs. 9–11, it is easy to find that both the macro- and micro-cracks are orthogonal to Y (tensile loading) direction. When heat flows into the specimen from Y direction, it will be blocked by ITR from conducting into the aggregates. Hence most of the heat flows into the mortar in order to bypass the cracked ITZ area (Fig. 13b). Correspondingly, when heat flows into the specimen from X direction, it can flow into the aggregates without thermal barriers, resulting in a little weakening of "heat bridge effect" (Fig. 13c). Therefore the T-ETCV reduces 23% and T-ETCP decreases 10%.

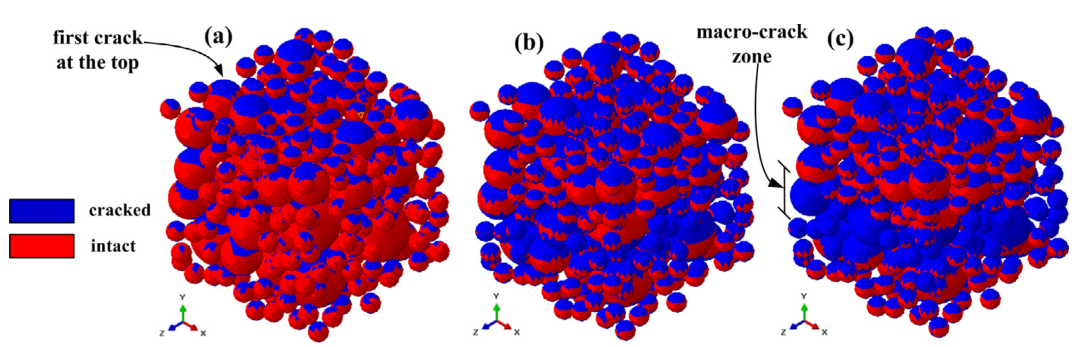

Fig. 11. Thermal conductivity distribution at ITZ during tensile test: (a) 76 μ-strain, (b) 100 μ-strain and (c) 500 μ-strain.

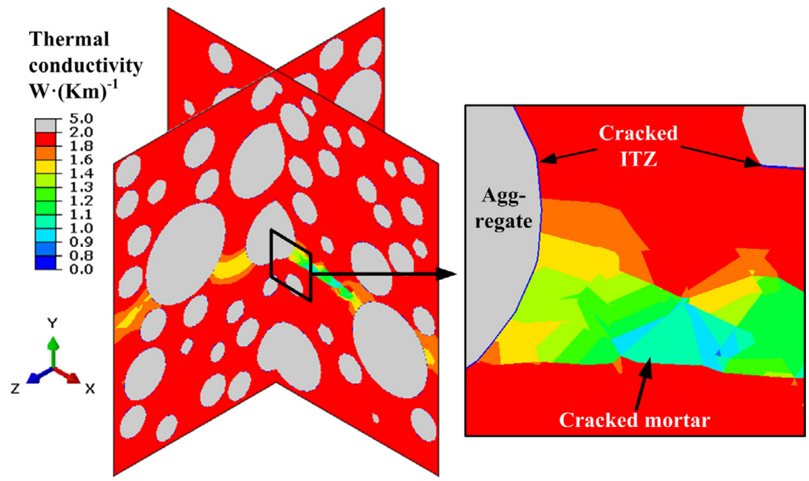

Fig. 12. Thermal conductivity distribution at tensile 500 μ-strain.

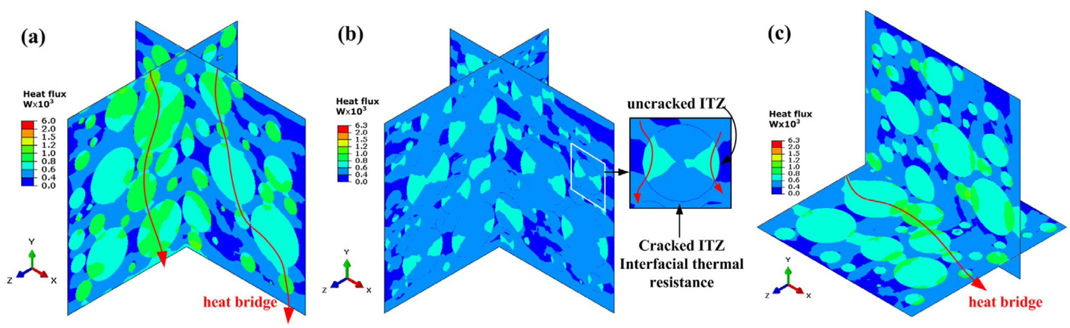

Fig. 13. Heat flux during tensile test: (a) ETC 0 μ-strain, (b) T-ETCV 500 μ-strain and (c) T-ETCP 500 μ-strain.

In summary, during the tensile failure process, the concrete ETC has a significant drop in the plastic stage due to the appearance of micro-cracks while in the softening stage it decreases slightly with the increase of macro-crack opening. Further, ETC becomes anisotropic because of the direction of cracks (or loading).

2.4.2. Compression

Fig. 14 shows the numerical complete compressive stress-strain curves (black) and the relationships between compressive strain and compressive cracked concrete ETC vertical to cracks (T-ETCV in red) or compressive cracked concrete ETC parallel to cracks (T-ETCP in blue) respectively. In the compressive stiffening stage (0–400 μ-strain), stress increases linearly with strain. As load increases, inelastic strains appear due to the initiation of micro-cracks at ITZ (Fig. 15) and during this apparent plastic stage (400–1600 μ-strain) discontinuity appears in the displacement distribution (Fig. 16b). At 1600 μ-strain, this specimen reaches the peak stress of 21 MPa at which almost all the ITZ elements are cracked (Fig. 15b). In softening stage, the stress decreases dramatically and the specimen is crushed into several parts (Fig. 16c). Overall, unlike the brittleness in tension, the compressive mechanical behavior is somewhat plastic.

The C-TECV and C-ETCP curves are made up of 4 stages, among which the plastic stage (400–1600 μ-strain) is divided into plastic drop stage (400–600 μ-strain) and plastic steady stage (600–1600 μ-strain). In the elastic period, these curves are overlapped. During the plastic drop stage, one can observe remarkable reductions in C-ETCV (30%) and C-ETCP (23%) and a bifurcation of these curves occurs at 500 μ-strain. Both curves become stable temporally during the plastic steady stage, and during the softening stage begins to linearly decrease.

It is noteworthy that micro-cracks initiate at ITZ at a 45-degree angle with respect to the Y (loading) direction as illustrated in Fig. 17a. With the increase of compressive deformation micro-cracks grow along the surface of aggregates and gradually cover the aggregates except for the top ends in the Y direction (Fig. 17b). That is the reason for the overlap and bifurcation of C-ETCV and C-ETCP curves mentioned above. A comparison between Fig. 17b and c indicates that the number of cracked ITZ elements is already saturated at the peak point.

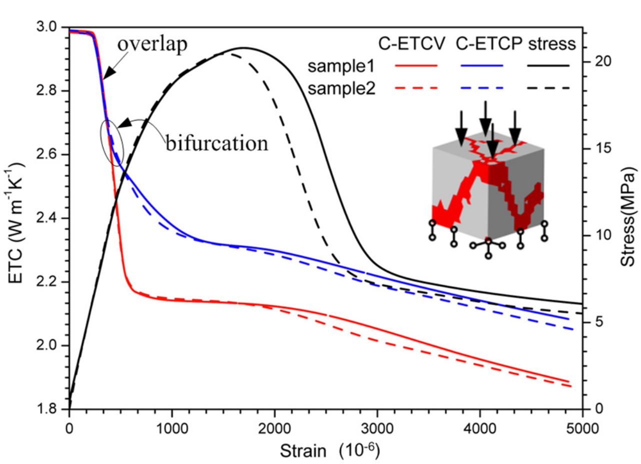

Fig. 14. Relationship between compressive strain and ETC.

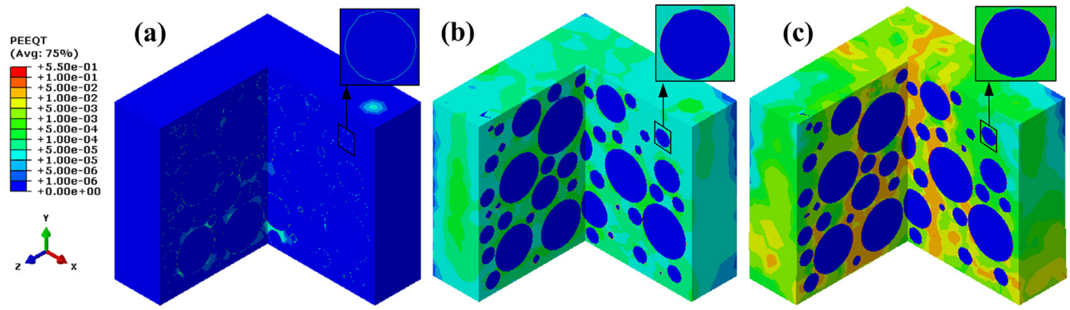

Fig. 15. PEEQT($\tilde{\varepsilon}_t^{ck}$ in ABAQUS) distribution at ITZ during compressive test: (a) 500 μ-strain, (b) 1600 μ-strain and (c) 5000 μ-strain.

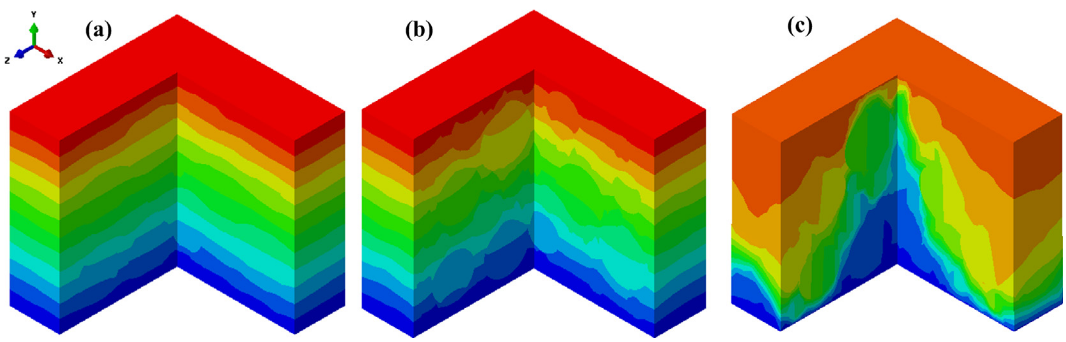

Fig. 16. Y-displacement distribution during compressive test: (a) 500 μ-strain, (b) 1600 μ-strain and (c) 5000 μ-strain.

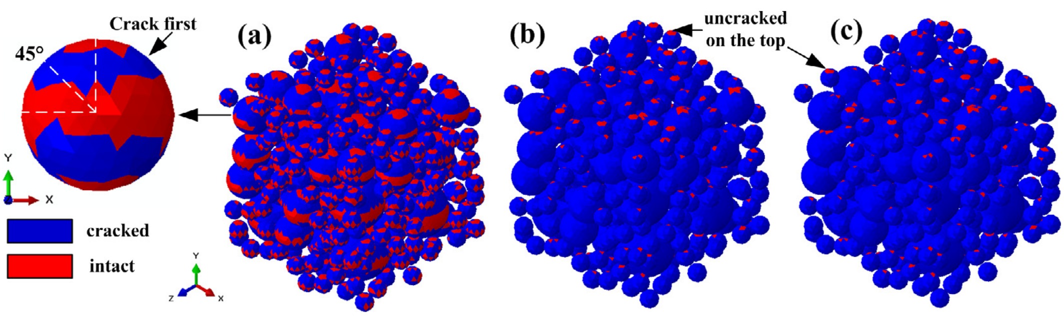

Fig. 17. Thermal conductivity distribution at ITZ during compressive test: (a) 500 μ-strain, (b) 1600 μ-strain and (c) 5000 μ-strain.

Fig. 18 shows the distribution of thermal conductivity in a compressed 5000 μ-strain concrete specimen. In this illustration, the thermal conductivity of elastic aggregate elements (gray), uncracked mortar and ITZ elements (red) remains unchanged, the conductivity of cracked ITZ elements turns into that of air and at the location of the macro-crack the conductivity of cracked mortar elements decreases to various degrees with crack opening. Also, one can observe several intertwined cracks inside the specimen in a manner that is completely different from the one single macro-crack in observed tensile cracked concrete.

Based on the discussion above, the ITR effect which prevents heat from flowing into aggregates clearly plays a dominant role in the reduction of thermal conductivity before the softening stage (see Fig. 19a, b, d and e). Then after the full growth (saturation number) of cracked ITZ elements, the crack-opening increase of intertwined macro-cracks causes a linear decrease of C-ETCV and C-ETCP which seems a little more apparent than that of the T-ETCV and T-ETCP curves. This could be observed by comparing the heat flux in mortar phase in Fig. 19b–c and e–f.

In conclusion, during the compressive failure process, the concrete ETC has a significant drop in the plastic drop stage due to the appearance of micro-cracks and in the softening stage it decreases linearly with the increase of macro-cracks opening. Furthermore, the ETC becomes anisotropic because of the direction of loading. C-ETCV and C-ETCP decrease 30% and 23%, respectively.

3. Experiment

This section discusses experiments in which the compression test and thermal conductivity measurements are carried out simultaneously. The most difficult task is to choose an appropriate method to obtain the temperature gradient without any interference with the mechanical results. The infrared thermal imaging, therefore, may be the most suitable approach which has been applied on a number of situations in concrete structures, such as bridges, highway and airport pavement [32,33]. Büyüköztürk [34] stated that this technology although was characterized by considerable accuracy and convenience, it could be affected significantly by change of weather condition. This drawback, however, is avoided in this study since all the operation is taken place in an indoor laboratory with controlled environment.

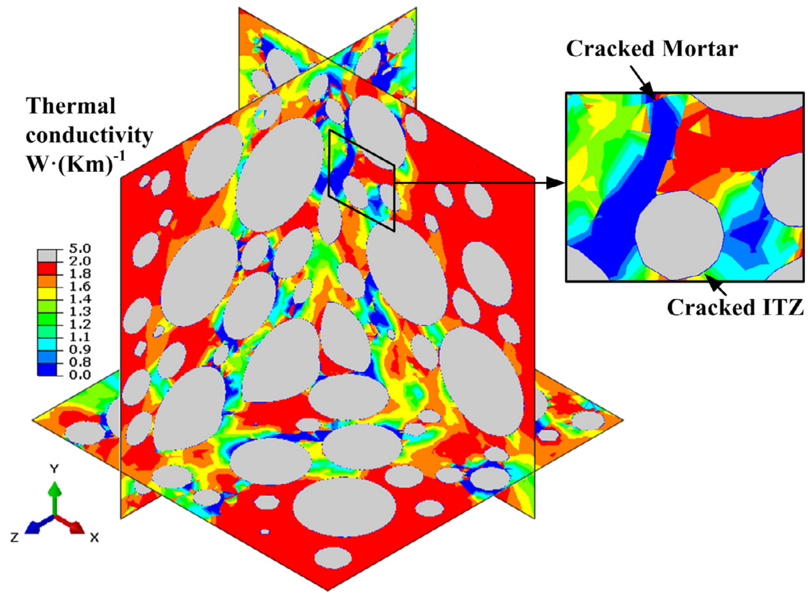

Fig. 18. Thermal conductivity distribution at compressive 5000 μ-strain.

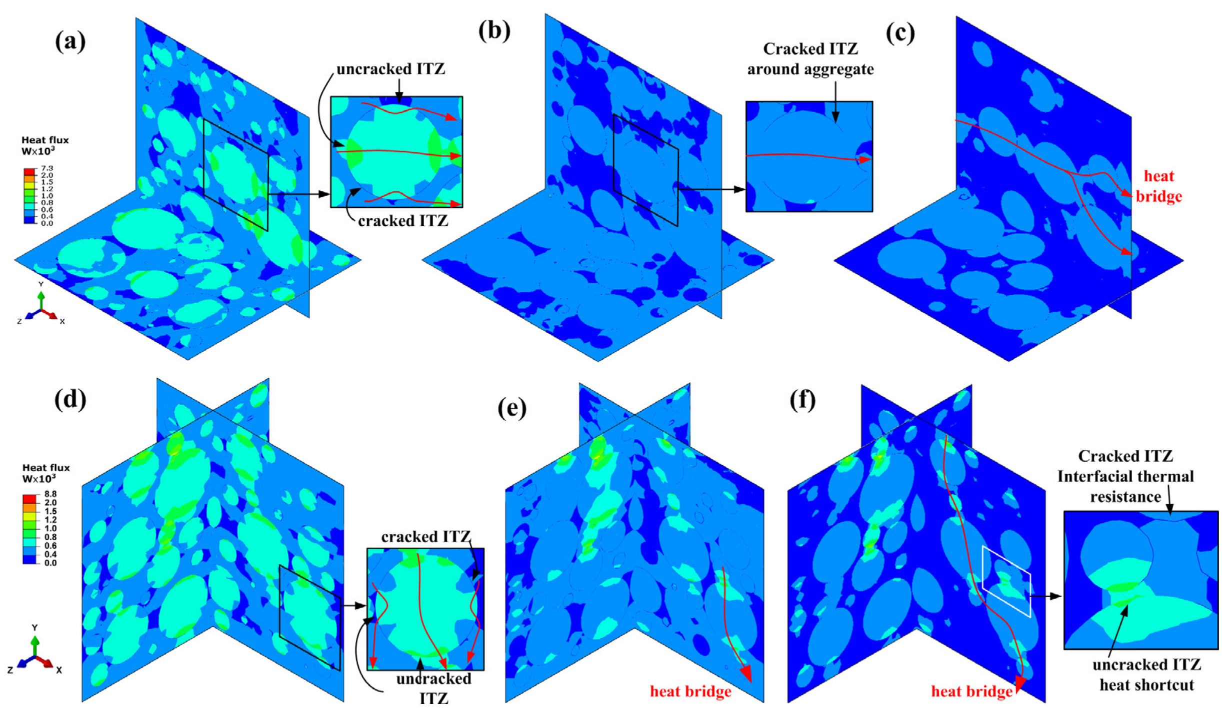

Fig. 19. Heat flux during compressive test: (a) C-ETCV 500 μ-strain, (b) C-ETCV 1600 μ-strain, (c) C-ETCV 5000 μ-strain, (d) C-ETCP 500 μ-strain, (e) C-ETCP 1600 μ-strain and (f) C-ETCP 5000 μ-strain.

Another difficulty is the measurement of discontinuous displacements and strain distribution on the specimen's surface with non-uniform temperature distribution. Here digital image correlation (DIC) [35,36] is employed to observe the failure process. DIC is a fully non-destructive and non-contact measurement tool which has been widely used to examine the deformation of engineering materials, including concrete and related cement-based materials.

The adopted setup is shown in Fig. 20 in which the infrared thermal imaging camera, whose thermal sensitivity is 0.04 °C and precision is 2%, is used to measure the temperature field on the concrete surface and the DIC, whose resolution is 1280 × 1024, is used to measure the discontinuous displacement and maximum principle strain distribution. The key point of this choice is that these approaches do not have any mutual interference. The measuring range of the electro-hydraulic servo universal testing machines (WAW-E2000) is 40–2000 kN which is capable of outputting persistent force to keep the specimen in a compressive status. The environmental temperature is kept at 25 °C and the humidity is not controlled.

3.1. Specimens

The compressive strength test in this experimental investigation strictly obeys the Chinese "Test Code for Hydraulic Concrete" (SL352-2006). The load speed is 0.3 MPa/s, and mix proportion is listed in Table 2. The six cubic specimens of 150 mm side length

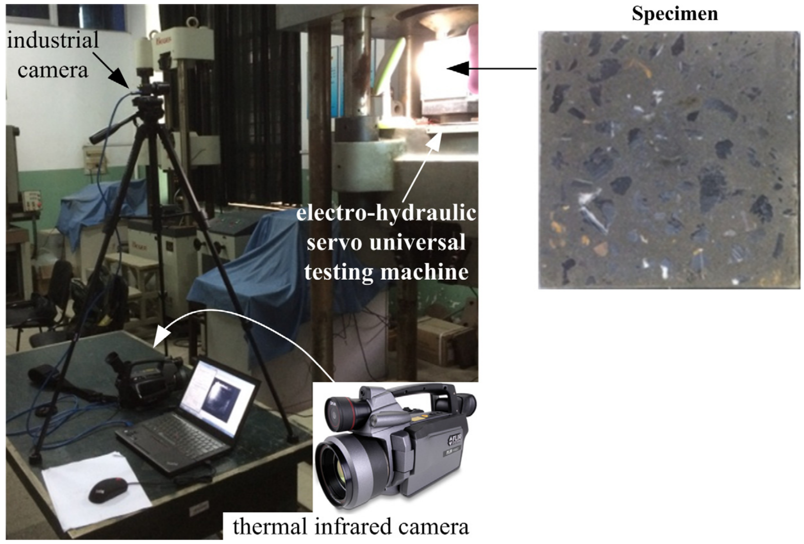

Fig. 20. Experiment setup.

Table 2
Component mass (kg) per m^3 C25 concrete.

Material		Component mass (kg)
Portland cement	P.O 32.5	380
Natural sand	middle	625
Crushed aggregates	diameter: 20–40 mm	1235
Water		200

are cured in water for 28 days and then the rough cast surface of each cube is polished in order to expose the aggregates (shown in Fig. 20). The natural different grayscale between aggregates and mortar can be used as the speckle pattern for DIC method.

3.2. Equipment

The equipment illustrated in Fig. 21a is designed based on the steady-state method which is detailedly described in the Chinese standard "Thermal Insulation-Determination of Steady-state Thermal Resistance and Related properties-Guarded Hot Plate Apparatus" (SL352-2006). Components are listed as follows: 1. Carbon steel frame (Q255); 2. Heat insulation foam board (0.002 $W{\cdot}K^{-1}\,m^{-1}$); 3. Heat insulation aluminosilicate fiber textile (0.035 $W{\cdot}K^{-1}\,m^{-1}$); 4. Concrete specimen; 5. Heating unit (electric heating silicon sheet, 15 W); 6. High thermal conductivity silicon sheet (6 $W{\cdot}K^{-1}\,m^{-1}$); 7. Cooling unit (water cooler); 8. Square carbon steel top plate with 150 mm side length; 9. Plate for supporting spring; 10. Carbon steel top frame; 11. Screw; 12. Spring.

Fig. 21b shows the operation schematic diagram. When load is applied to the top plate (8), expansion strain will appear in the direction orthogonal to the loading direction, because of the deformation and cracks inside the specimen (4). Then, the springs (12) supported by fixed plates (9) will shrink due to the movement of the foam boards (4), the heating unit (5) and the cooling unit (7). The heating unit (5) provides a stable heat source on one surface and the cooling unit keeps another parallel surface at room temperature. Hence during loading is kept, a steady heat flow forms inside the specimen (4) and a temperature gradient ∇T can be obtained between the two parallel surfaces after sufficient time. Thus the specimen's C-ETCV can be computed as:

$$\lambda_{exp} = \frac{Q}{\nabla T \cdot l} \tag{11}$$

where l is the side length of cubic specimen and Q is the steady heat flow which depends on the heating unit's electricity consumption, W, and its heat efficiency. Because of some uncontrollable factors, such as heat leak, precision of instruments and so on, a correction factor, k_{exp}, considering heat efficiency is defined for this equipment:

$$\lambda_{exp} = k_{exp} \frac{W}{\nabla T \cdot l} \tag{12}$$

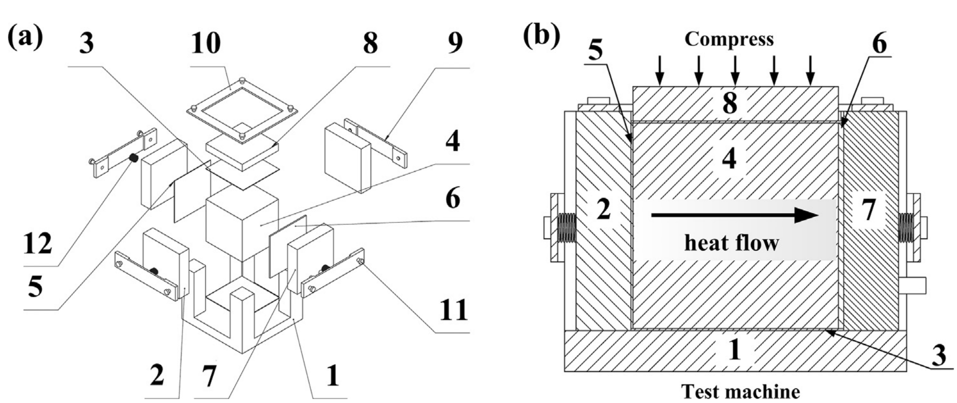

Fig. 21. Illustrations of Equipment: (a) Exploded views and (b) Operation schematic diagram.

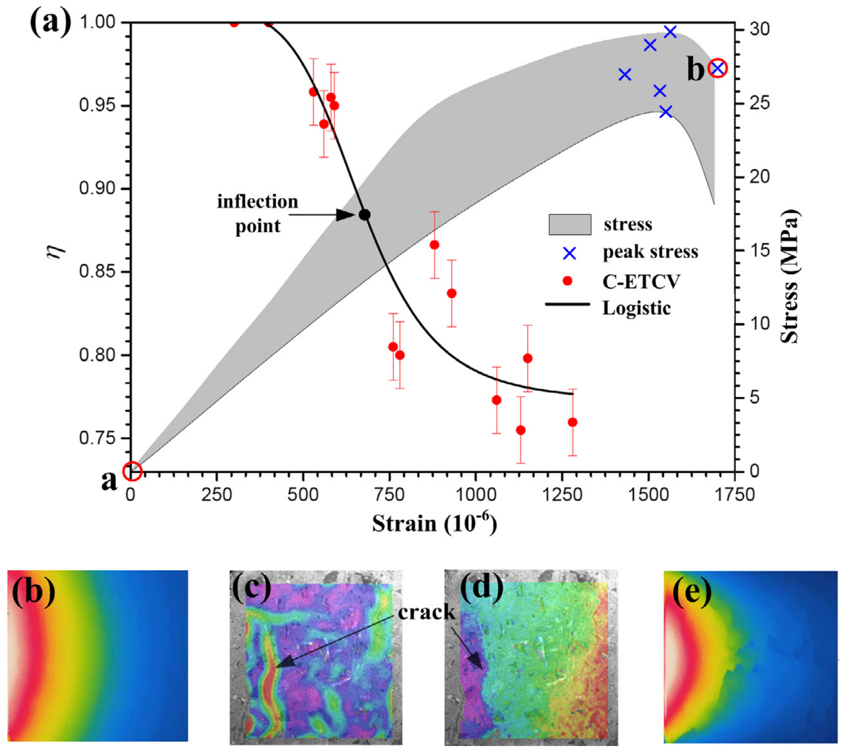

Fig. 22. Percentage of thermal conductivity during the uniaxial compression test: (a) Experimental data, (b) Temperature at point a, (c) Maximum principle strain at point b, (d) Displacement at point b, and (e) Temperature at point b.

3.3. Experimental results

4 sets of valid data are plotted in Fig. 22a. The elasticity modulus ranges from 19.3 to 28.8 GPa, the compressive strength ranges from 24.5 to 29.2 MPa and the reduction of C-ETCV ranges from 21% to 25%. The scatter of elasticity modulus may be caused by alteration of cooling water temperature in different experimental days, because the elasticity modulus is sensitive to average temperature of specimen [37]. To begin with, one needs to measure the steady temperature distribution of the intact specimen (point a in Fig. 22a). In Fig. 22b, one can see a uniform one-dimensional temperature gradient ∇T^{un}. During the test, specific compressive loads (0 MPa, 10 MPa, 15 MPa, 20 MPa and 25 MPa) are successively applied and held, and whereafter the temperature of the two parallel surfaces' center points are monitored until a new steady gradient ∇T^{ck} is reached. At the peak compressive stress (point b in Fig. 22a), macro-cracks (Fig. 22c) and discontinuous displacement distribution (Fig. 22d) can be observed on the surface of the concrete specimen. In addition, when damage localizes, temperature discontinuities can be observed in Fig. 22e. It is important to point out that this temperature distribution cannot be used to calculate the conductivity, because it is transient. Also the neither before or after cracking temperature distributions are not ideal one-dimensional along the temperature gradient (from left to right in Fig. 22b and e), because a certain amount of heat leaks from top and bottom (aluminosilicate fiber textile in Fig. 21), even though its thermal conductivity is very low (0.035 W·K^{-1} m^{-1}). In order to avoid this drawback, the reduction proportion of conductivity η is used to eliminate k_{exp} which cannot be measured accurately:

$$\eta = \frac{\lambda_{\mathrm{eff}}^{\mathrm{ck}}}{\lambda_{\mathrm{eff}}^{\mathrm{un}}} = \frac{W^{\mathrm{ck}} \nabla T^{\mathrm{un}}}{W^{\mathrm{un}} \nabla T^{\mathrm{ck}}} \tag{13}$$

where $\lambda_{\mathrm{exp}}^{\mathrm{ck}}$ and $\lambda_{\mathrm{exp}}^{\mathrm{un}}$ are the experimental thermal conductivity of uncracked and cracked concrete, respectively; W^{un} and W^{ck} are the power consumptions of the heating unit (5) for the uncracked and cracked concrete respectively. Therefore the reductions of C-ETCV under various compressive loads can be obtained which is plotted in Fig. 22a as the red nodes.

The simulations in Section 2.4.2 show that the C-ETCV has a significant reduction during plastic drop stage and then it becomes steady until the specimen reaches its peak stress. For this reason, this curve presents an "S" shape. Hence the Logistic function is employed to fit the experimental data:

$$\eta = \frac{\eta_{\max} - \eta_{\min}}{1 + (\varepsilon/\varepsilon_{\mathrm{p}})^{p}} + \eta_{\min} \tag{14}$$

The Logistic curve is composed of a convex function ($\varepsilon < \varepsilon_{\mathrm{p}}$), a concave function ($\varepsilon > \varepsilon_{\mathrm{p}}$) and an inflection point p ($\varepsilon = \varepsilon_{\mathrm{p}}$), in which parameter p is related to the slope at point p; $\eta_{\max}$ and $\eta_{\min}$ is the maximum and minimum of this function. The fitted curve is plotted as the black line in the Fig. 22a and its parameters are listed in Table 3. The fitted curve shows a significant decrease at 400–800 μ-strain and becomes stable at 800–1250 μ-strain. This phenomenon confirms the definition of plastic steady stage and plastic drop stage in compressive numerical test.

4. Semi-theoretical model

According to the simulations, the debonding of aggregates and mortar plays a dominant role in ETC reduction during concrete failure. Hence homogenization model for cracked concrete ETC should consider the cracked ITZ (air). However cracked ITZ is not uniformly mixing in mortar matrix which means three-phase homogenization model is not suitable in this study. It is more proper to assume the cracked ITZ as the interfacial thermal resistance in two-phase composite (aggregates and mortar). Therefore the following model is recommended.

Table 3
Values of Logistic function fitting parameters.

parameter	η_{max}	η_{min}	ε_p (μ-strain)	p
value	1	0.76	669	6.19

Based on the pioneering work of Maxwell [38], many semi-theoretical models with succinct forms and explicit physical meaning for two-phase composite materials have been developed by taking into account more influencing factors. Bruggeman [39] model took the effect of high particle content into account. Hamilton-Crosser model [40] considered the effect of particle shapes. Hasselman-Johnson model [41] was capable of including the effect of interfacial thermal resistance. Based on existing fruitful results, Wang [42] presented an advanced Maxwell model (Wang model) which featured the effect of particle shape, ITR and high particle content:

$$(1-v_p)^n = \left(\frac{\lambda_m}{\lambda_{eff}}\right)^{(1+n\alpha-\alpha)/(1-\alpha)} \left(\frac{\lambda_{eff}-\lambda_p(1-\alpha)}{\lambda_m-\lambda_p(1-\alpha)}\right)^{n/(1-\alpha)} \tag{15}$$

where λ_m and λ_p stand for the thermal conductivity of continuous phase (mortar matrix) and discrete phase (aggregates), receptively; v_p is the particle volume fraction, i.e., AVF; $n \in (1,3]$ is particle shape factor which is related to the particle's sphericity. For spherical particles, n equals to 3; $\alpha \in (0,1]$ presents the degree of ITR effect. $\alpha = 0$ means no ITR effect, $\alpha < 1$ means the increase of v_p has a negative effect on material ETC and conversely $\alpha > 1$ indicates a positive effect on ETC. Zhang et al. [43] verified the feasibility of applying of above models to estimate concrete ETC by comparing with experiment data.

As a matter of fact, all the methods, namely simulations, experiments and semi-theories, are not perfect. The drawback of FEM simulations is the low AVF (around 40%) of mini-scale numerical specimens while in engineering concrete AVF ranges from 50% to 70%. The disadvantages of experiments are the complex operating procedures and the lost of ETC evolution during post-peak softening. Regarding Wang model, its accuracy completely relies on the selection of parameters which depend on the ratio of two phases' thermal conductivity, moisture condition and other factors. As all these influences are stochastic and complicate in concrete, the pure theoretical determination of n and α is rather difficult. To address this problem, the numerical results in Section 2.4 which are regarded as known data are used to calibrate the unknown coefficient, namely aggregate shape factor n and ITR factor α, by following the least square method. Then a comparison between Wang model and experimental data is carried out to verify the reliability of simulations.

Consider now that the ITR factor, α, changes with failure model while keeping the shape factor, $n = 3$, constant as aggregates are spheres in simulations. For intact concrete specimens which means $\alpha = 0$, one can find in Fig. 23 Wang model agrees (black line) well with numerical results (red nodes). Regarding the compressive cracked specimens, when α equals to 0.478 and 0.337 respectively, Wang model (red and blue line) matches well with C-ETCV (green nodes) and C-ETCP (blue nodes). And for the tensile cracked specimens, when α equals to 0.337 and 0.094 respectively, Wang model (blue and green line) matches well with T-ETCV (purple nodes) and T-ETCP (dark blue nodes). Notice that the cracked concrete ETC is the value of conductivity at the specimens' peak stress point since the ITR effect plays a dominant role.

In Fig. 24, a comparison of cracked concrete ETC percentage between Wang model and experimental data is presented. In the high AVF range (70–75%), Wang model matches well with Vejmelkov et. al.'s [4] experiment which adequately makes up for

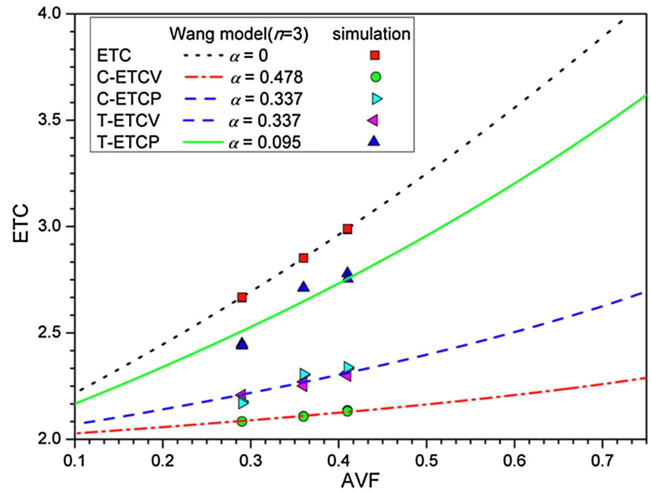

Fig. 23. Wang Model fit of simulation results.

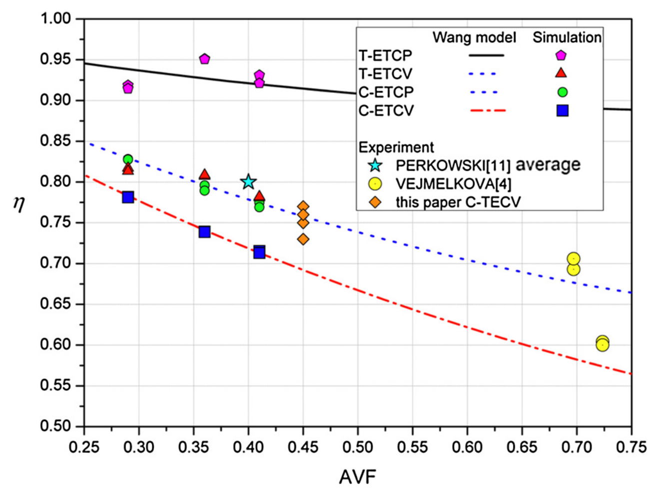

Fig. 24. Comparison of ETC percentage.

the disadvantages of the low AVF of mini-scale specimens used in simulations. However Wang model does not achieve a satisfactory fit of test data in this investigation (orange points). This may be caused by various factors, such as the difference of components' thermal conductivity, aggregates' shape [9] and so on.

In Figs. 23 and 24, AVF shows a significant impact on both intact concrete ETC and cracked concrete ETC. In Fig. 23, concrete ETC increases with AVF, since more aggregates can provide "heat bridge" for heat. In Fig. 24, the reduction of ETC due to cracking increases with AVF because the more ITR effect arise during failure. This is completely consistent with two-dimensional simulations [9].

5. Conclusions

A mini-scale numerical method is proposed within the framework of finite element method (ABAQUS) to simulate the thermal conductivity of both tensile and compressive cracked concrete with 50 μm Interfacial Transition Zone (ITZ) in 3-D. The main conclusions are as follows:

(1) In the course of the tensile failure process, the evolution between ETC (effective thermal conductivity), including T-ETCV (tensile cracked concrete ETC vertical to cracks) and

T-ETCP (tensile cracked concrete ETC parallel to cracks), and strain can be divided into 3 stages. In the elastic stage, ETC has a little change. In plastic stage (80–100 μ-strain) both the ETCV (23%) and ETCP(10%) has a significant reduction. In the softening stage a very slight linear decrease occurs.

(2) According to the compressive failure process the C-TECV (compressive cracked concrete ETC vertical to cracks) and C-ETCP (compressive cracked concrete ETC parallel to cracks) curves are made up of 4 stages. In the elastic stage, tow curves have no change and are overlapped. Then at plastic drop stage, one can observe remarkable reductions in C-ETCV (30%) and C-ETCP (23%) and a bifurcation of the curves at 500 μ-strain. As load increases both curves become stable temporally during the plastic steady stage, and during the softening stage then begin to linearly decrease again.

(3) It is the micro-cracks at Interfacial Transition Zone (ITZ) rather than the macro-cracks that play the dominant role in this phenomenon. Aggregate particles whose thermal conductivity is commonly 2.5 times of that of mortar provides "heat bridges" for heat transfer. The micro-cracks induced by the debonding of mortar and aggregates prevent heat flowing into the aggregates which remarkably weakens the heat bridge effect. This is called interfacial thermal resistance (ITR) effect.

Experiments conducted in this study show that C-ETCV dramatically decreases 20–25% at 300–900 micro compressive strain and then becomes steady. This phenomenon confirms the conceptions of plastic drop stage and plastic steady stage which are defined in simulations, indicating the correctness of simulations.

Wang model which is calibrated by simulations is recommended to estimate the ETC of cracked concrete. The agreement between the data from simulations, Wang model and experiment indicates the correctness of this study.

However, further researches need to be carried out. Better constitutives, such as lattice discrete particle model [18] or fracture constitutive [8], need to be employed to model more explicit cracking pattern and failure phenomena. The ETC evolutions during the complex mechanical and thermal load, and the improvements of aggregate volume fraction (AVF) for both numerical and real specimen are essential for the application in engineering. It is, as well, of interest to account for the effects of the concrete mixture, moisture content and high temperature condition on cracked concrete ETC.

Acknowledgements

The research presented in this paper was supported by the National Nature Science Foundation of China (Grant No. 11132003), the Fundamental Research Funds for the Central Universities (Hohai University, 2013/B15020334) and scholarship from China Scholarship Council (201606710080). The work of Prof. Cusatis was supported in part under Grant NRC-HQ-60-14-FOA-0001 to Northwestern University.

The computing services were provided by the High Performance Computing Center of Hohai University. The infrared thermal imaging was provided by State Key Laboratory of Hydrology-water Recourses and Hydraulic Engineering of Hohai University. The industrial camera was provided by the Department of Engineering Mechanics of Hohai University.

The authors would like to express their appreciation to the faculty of the Department of Engineering Mechanics of Hohai University, namely Jingrong Wang, Prof. Dong Lei, Lecturer Feipeng Zhu and Prof. Shanshan Wang.

References

[1] J. Pan, J. He, Large Dams in China: A Fifty-Year Review, China Water Power Press, 2000.
[2] B.F. Zhu, Thermal Stresses and Temperature Control of Mass Concrete, China Water & Power Press, 2012.
[3] V. Kodur, W. Khaliq, Effect of temperature on thermal properties of different types of high-strength concrete, J. Mater. Civil Eng. 23 (6) (2011) 793.
[4] E. Vejmelkova, P. Padevet, R. Cerny, Effect of cracks on hygric and thermal characteristics of concrete, Bauphysik 30 (6) (2008) 438–444.
[5] T.S. Yun, Y.J. Jeong, K.S. Youm, Effect of surrogate aggregates on the thermal conductivity of concrete at ambient and elevated temperatures, Sci. World J. 2014 (2014) 939632.
[6] S.B. Tang, C.N. Tang, Z.Z. Liang, Y.B. Zhang, L.C. Li, Numerical study of the influence of material structure on effective thermal conductivity of concrete, Heat Transfer Eng. 33 (8) (2012) 732–747.
[7] Y.F. Fu, Y.L. Wong, C.A. Tang, C.S. Poon, Thermal induced stress and associated cracking in cement-based composite at elevated temperatures––Part II: thermal cracking around multiple inclusions, Cem. Concr. Compos. 26 (2) (2004) 113–126.
[8] Y.F. Fu, Y.L. Wong, C.A. Tang, C.S. Poon, Thermal induced stress and associated cracking in cement-based composite at elevated temperatures––Part I: Thermal cracking around single inclusion, Cem. Concr. Compos. 26 (2) (2004) 99–111.
[9] L. Shen, Q. Ren, N. Xia, L. Sun, X. Xia, Mesoscopic numerical simulation of effective thermal conductivity of tensile cracked concrete, Constr. Build. Mater. 95 (2015) 467–475.
[10] T. Wu, P. Wriggers, Multiscale diffusion–thermal–mechanical cohesive zone model for concrete, Comput. Mech. 55 (5) (2015) 999–1016.
[11] Z. Perkowski, Change of thermal conductivity of concrete caused by brittle damage evolution, Bauphysik 30 (6) (2008) 434–437.
[12] P. Wriggers, S.O. Moftah, Mesoscale models for concrete: Homogenisation and damage behaviour, Finite Elem. Anal. Des. 42 (7) (2006) 623–636.
[13] W. She, Y.S. Zhang, M.R. Jones, Three-dimensional numerical modeling and simulation of the thermal properties of foamed concrete, Constr. Build. Mater. 50 (2014) 421–431.
[14] J.Z. Xiao, W.G. Li, D.J. Corr, S.P. Shah, Effects of interfacial transition zones on the stress-strain behavior of modeled recycled aggregate concrete, Cem. Concr. Res. 52 (2013) 82–99.
[15] C.B. Du, L.G. Sun, S.Y. Jiang, Z.Q. Ying, Numerical simulation of aggregate shapes of three-dimensional concrete and its applications, J. Aerosp. Eng 26 (3) (2013) 515–527.
[16] G. Cusatis, Z.P. Bažant, L. Cedolin, Confinement-shear lattice CSL model for fracture propagation in concrete, Comput. Methods Appl. Mech. Eng. 195 (52) (2006) 7154–7171.
[17] G. Cusatis, A. Mencarelli, D. Pelessone, J. Baylot, Lattice discrete particle model (LDPM) for failure behavior of concrete. II: calibration and validation, Cem. Concr. Compos. 33 (9) (2011) 891–905.
[18] G. Cusatis, D. Pelessone, A. Mencarelli, Lattice discrete particle model (LDPM) for failure behavior of concrete. I: theory, Cem. Concr. Compos. 33 (9) (2011) 881–890.
[19] R. Rezakhani, G. Cusatis, Asymptotic expansion homogenization of discrete fine-scale models with rotational degrees of freedom for the simulation of quasi-brittle materials, J. Mech. Phys. Solids 88 (2016) 320–345.
[20] Hibbitt, Karlsson, Sorensen, ABAQUS Theory Manual, Dassault Systèmes, 2012.
[21] S.M. Kim, R.K. Abu Al-Rub, Meso-scale computational modeling of the plastic-damage response of cementitious composites, Cem. Concr. Res. 41 (3) (2011) 339–358.
[22] X.L. Du, L. Jin, G.W. Ma, Numerical simulation of dynamic tensile-failure of concrete at meso-scale, Int. J. Impact Eng. 66 (2014) 5–17.
[23] J. Lubliner, J. Oliver, S. Oller, E. Oñate, A plastic-damage model for concrete, Int. J. Solids Struct. 25 (3) (1989) 299–326.
[24] J.H. Lee, G.L. Fenves, Plastic-damage model for cyclic loading of concrete structures, J. Eng. Mech.-ASCE 124 (8) (1998) 892–900.
[25] W. Tao, Numerical Heat Transfer, Xi'an Jiaotong University Press, Xi'an, 2001.
[26] J. Skrzypek, A. Ganczarski, Modeling of Material Damage and Failure of Structures: Theory and Applications, Springer Science & Business Media, 2013.
[27] J. Xiao, W. Li, Z. Sun, D.A. Lange, S.P. Shah, Properties of interfacial transition zones in recycled aggregate concrete tested by nanoindentation, Cem. Concr. Compos. 37 (2013) 276–292.
[28] P.E. Petersson, Fracture energy of concrete: practical performance and experimental results, Cem. Concr. Res. 10 (1) (1980) 91–101.
[29] L. Shuguang, L. Qingbin, Method of meshing ITZ structure in 3D meso-level finite element analysis for concrete, Finite Elem. Anal. Des. 93 (2015) 96–106.
[30] Y. Xu, S. Chen, A method for modeling the damage behavior of concrete with a three-phase mesostructure, Constr. Build. Mater. 102 (2016) 26–38.
[31] O.L. Manzoli, M.A. Maedo, L.A.G. Bitencourt, E.A. Rodrigues, On the use of finite elements with a high aspect ratio for modeling cracks in quasi-brittle materials, Eng. Fract. Mech. 153 (2016) 151–170.
[32] M.R. Clark, D.M. McCann, M.C. Forde, Application of infrared thermography to the non-destructive testing of concrete and masonry bridges, NDT E Int. 36 (4) (2003) 265–275.
[33] G.J. Weil, Non-destructive testing of bridge, highway and airport pavements, 1992.

[34] O. Büyüköztürk, Imaging of concrete structures, NDT E Int. 31 (4) (1998) 233–243.
[35] D. Corr, M. Accardi, L. Graham-Brady, S. Shah, Digital image correlation analysis of interfacial debonding properties and fracture behavior in concrete, Eng. Fract. Mech. 74 (1–2) (2007) 109–121.
[36] S. Choi, S.P. Shah, Measurement of deformations on concrete subjected to compression using image correlation, Exp. Mech. 37 (3) (1997) 307–313.
[37] S.N. Shoukry, G.W. William, B. Downie, M.Y. Riad, Effect of moisture and temperature on the mechanical properties of concrete, Constr. Build. Mater. 25 (2) (2011) 688–696.
[38] J.C. Maxwell, A Treatise on Electricity and Magnetism, Clarendon press, 1881.
[39] D. Bruggeman, Calculation of various physics constants in heterogenous substances I Dielectricity constants and conductivity of mixed bodies from isotropic substances, Ann. Phys. 24 (7) (1935) 636–664.
[40] R.L. Hamilton, O.K. Crosser, Thermal conductivity of heterogeneous two-component systems, Ind. Eng. Chem. Fundam. 1 (3) (1962) 187–191.
[41] D.P.H. Hasselman, L.F. Johnson, Effective Thermal Conductivity of Composites with Interfacial Thermal Barrier Resistance, J. Compos. Mater. 21 (6) (1987) 508–515.
[42] J.J. Wang, Preparatin and Investigation on the Polyimide/AIN Composite Materials, Zhejiang University, 2001.
[43] W.P. Zhang, H.G. Min, X.L. Gu, Y.P. Xi, Y.S. Xing, Mesoscale model for thermal conductivity of concrete, Constr. Build. Mater. 98 (2015) 8–16.